

# A General Cone-Beam Reconstruction Algorithm

Ge Wang, Tein-Hsiang Lin, Ping-chin Cheng, and Douglas M. Shinozaki

**Abstract**—Considering the characteristics of the x-ray microscope system being developed at SUNY at Buffalo and the limitations of available cone-beam reconstruction algorithms, a general cone-beam reconstruction algorithm and its several special versions are proposed and validated by simulation. Our cone-beam algorithm allows various scanning loci, handles reconstruction of rod-shaped specimens which are common in practice, and facilitates near real-time reconstruction by providing the same computational efficiency and parallelism as Feldkamp's algorithm [1].

Although our cone-beam algorithm is not exact, it consistently gives satisfactory reconstructed images. Furthermore, it has several nice properties if the scanning locus meets some conditions. First, reconstruction within a midplane is exact using a planar scanning locus. Second, the vertical integral of a reconstructed image is equal to that of the actual image. Third, reconstruction is exact if an actual image is independent of rotation axis coordinate  $z$ . Also, the general algorithm can uniformize and reduce  $z$ -axis artifacts, if a helix-like scanning locus is used.

## I. INTRODUCTION

**A**N X-RAY shadow projection microscope system using a scannable x-ray point source is under development at AMIL-ARTS (SUNY at Buffalo) for acquiring three-dimensional micro-images, which are very useful in the study of biological and synthetic materials [2]–[9] (Fig. 1). The x-ray microscope system uses an electron optical column to produce a small, intense, and steerable electron spot, which in turn creates an x-ray spot of sufficient brightness to illuminate a specimen to resolve the structures of interest. The resolution of this x-ray microscope system is limited by the size of the x-ray spot due to penumbral blurring, which can be minimized by reducing the lateral spread of the electron beam in the target material [3]. The specimen is on the side of the target away from the electron beam. This permits the electron beam to be in vacuum while the specimen can sit in air or in an environmental chamber. To obtain the needed magnification,

Manuscript received November 14, 1991; revised September 10, 1992.

G. Wang is with the Division of Radiology Research, Mallinckrodt Institute of Radiology, Washington University, St. Louis, MO 63110.

T. H. Lin and P. C. Cheng are with the Advanced Microscopy and Imaging Laboratory (AMIL), and Advanced Real Time System Laboratory (ARTS), Department of Electrical and Computer Engineering, Center for Electronic and Electrooptics Materials (CEEM), State University of New York, Buffalo, NY 14260.

D. M. Shinozaki is with the Department of Materials Engineering, Faculty of Engineering Science, University of Western Ontario, London, Ontario, Canada N6A 5B7.

This work was supported by grants from the U.S. National Institute of Health—Biomedical Research Grant Program (BRSG SO7 RR07066), the U.S. National Science Foundation (NSF MIP-9010948), the U.S. Department of Energy (DE-AS08-88DP10782, DE-FG03-89SF18012), the Whitaker Foundation (Program for Biomedical Engineering); and by the NSERC (Canada) (Operating and Strategic grants), the Ontario Center for Materials Research, and the Canadian Synchrotron Radiation Facility (CSRF).

IEEE Log Number 9210288.

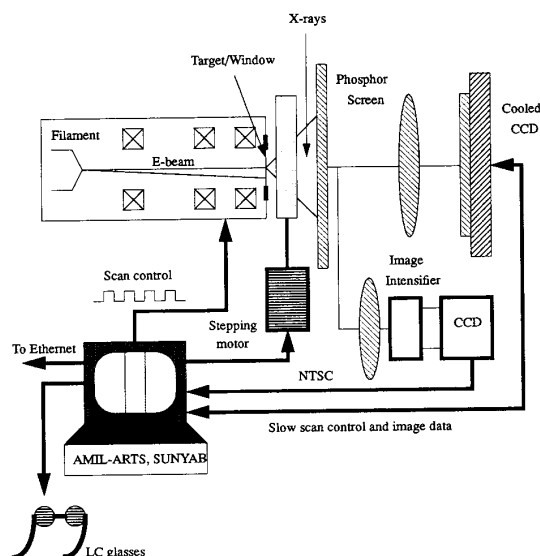


Fig. 1. The schematic diagram showing the x-ray shadow projection microscope being developed at SUNY at Buffalo.

the specimen must be placed close to the source, in this case, in the range of 0.1–1 mm. An x-ray projection image is obtained by placing a phosphor screen as the x-ray scintillator at a large distance from the specimen. The larger the distance, the higher the magnification, but the lower the image intensity. A two-dimensional slow-scanned CCD array (Kodak 1400) is used to grab the projection image formed on the screen. For microtomography, a series of such images is acquired at different orientations, and then processed for reconstruction. This approach is commonly called cone-beam reconstruction, as x-rays irradiating to a sphere-like specimen form a cone (Fig. 2).

Because none of the currently available cone-beam reconstruction algorithms are fully satisfactory for our x-ray microscope system, we will propose in this paper a general cone-beam algorithm which can be considered as a generalization of Feldkamp's algorithm [1]. Currently available cone-beam reconstruction algorithms are briefly reviewed in Section II. A heuristic mathematical derivation of the proposed general cone-beam algorithm is given in Section III. In Section IV, several interesting special versions of our cone-beam algorithm are studied. Analytic properties of our cone-beam algorithm are discussed in Section V.

## II. REVIEW OF CONE-BEAM ALGORITHMS

The cone-beam reconstruction of x-ray images has been studied for more than thirty years. The algorithms can be eval-

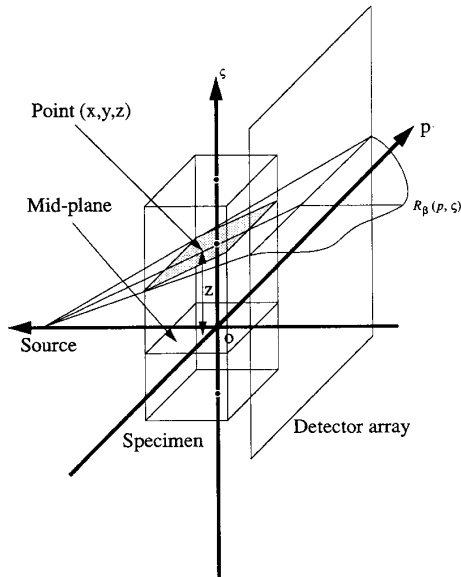


Fig. 2. Cone-beam reconstruction arrangement.

uated from various viewpoints, such as theoretical precision, computational efficiency, scanning geometry, and reconstruction region. A recent review was written by Smith [10].

Existing cone-beam algorithms can be categorized into two broad classes: analytic and algebraic [11], [12]. Algebraic algorithms demand more computing resources than analytic ones. Because a high reconstruction speed is very important in practice, analytic algorithms are always preferred.

Kirillov [13] developed an analytic formula for reconstructing a complex valued function in an  $n$ -dimensional complex space using complex valued cone-beam projection data. Kirillov assumed that the vertex describes an unbounded curve and showed that a sufficient condition for reconstruction in the Schwartz space is that the curve intersects almost every hyperplane. Tuy [14] modified Kirillov's approach and gave a reconstruction formula for functions of compact support when the curve is bounded, provided that almost every hyperplane meeting the support of the unknown function meets the curve at some point. Tuy derived a cone-beam reconstruction formula for two intersecting source circles, which requires a gradient to be computed at each vertex point. Hamaker *et al.* [15] discussed an approximate approach for cone-beam reconstruction when there are a finite number of source points available. These results are theoretically oriented and not directly applicable in practice.

Nalcioğlu and Cho [16] and Denton *et al.* [17] presented convolution-backprojection methods requiring that source positions encompass a sphere. The analytic results obtained by K. T. Smith [18], [19], Imiya [20], and Peyrin [21] are also based on the assumption of a sphere of "vertex points." However, it is very difficult to implement such a geometry, particularly in our x-ray microscope system.

Herman [22], and Lewitt and McKay [23], studied the unmodified fan-beam algorithm for cone-beam reconstruction.

When the cone angle is small, as in the scanner developed at the Mayo Clinic [24], the convolution-backprojection procedure works quite well. Grangeat's algorithm [25], [26] is also in the form of convolution-backprojection, where the planar integral values are estimated for three-dimensional Random inversion. Then, Sire, Grangeat, and Rizo *et al.* [27] developed a software package named RADON. Feldkamp *et al.* [1] proposed a practical cone-beam algorithm, which is an extension of the conventional equispacial fan-beam reconstruction algorithm, where two-dimensional projection data from different angles are filtered and backprojected to voxels along projection beams. The final value of each voxel is the sum of contributions from all tilted fan-beams passing through the voxel. Jaszczak's group and Gullberg's group also studied approximate filtering and backprojection cone-beam reconstruction [28]–[31].

Gullberg *et al.* [28], [29] and Wang *et al.* [32] independently studied Feldkamp's algorithm for planar noncircular scanning loci in different ways. Wang's heuristically derived formula is the same as Feldkamp's, except that the source-to-origin distance depends on the rotation angle, which is a special case of our cone-beam algorithm presented in this paper. Gullberg's formula contains a derivative of scanning locus resulted from the Jacobian transform, while Wang's formula does not contain such a derivative.

A thorough theoretical analysis on cone-beam reconstruction was done by Smith [10], [33]–[36]. He contributed the necessary and sufficient conditions for exact cone-beam reconstruction and the corresponding reconstruction methods. His algorithms are generally used in "complete" geometries and are less efficient than Feldkamp's algorithm, which is applied to data collected from a circle, a typical case of incomplete scanning geometries. Although his most computationally efficient algorithm is as efficient as Feldkamp's algorithm, it is based on the following assumption of imaging geometry: *Considering any line that contains a vertex point (a position of the x-ray source) and a reconstruction point, there is an integer  $M$  (which remains constant for this line) such that almost every plane that contains this line intersects the geometry exactly  $M$  times.* Known practical loci cannot meet this requirement. Actually, the only known curve that satisfies this condition is an infinitely long straight line extended in both directions.

Among various approaches, Feldkamp's heuristically derived algorithm is the most efficient and most suitable to parallel processing. For cone-beam x-ray microtomography, the main drawbacks of Feldkamp's algorithm, shortcomings of most of other algorithms as well, are that a specimen must be contained in a sphere-like reconstruction region and that the x-ray source must be moved along a circle in the specimen coordinate system. In addition, Feldkamp's algorithm suffers from a larger inaccuracy in reconstructing off-midplane structures.

### III. HEURISTIC DERIVATION OF GENERAL CONE-BEAM ALGORITHM

Our cone-beam algorithm is derived by modifying the convolution and backprojection algorithm for equispacial fan-

beam data. The locus of the x-ray source is described in a cylindrical coordinate system  $(\rho(\beta), h(\beta), \beta)$ , where  $\beta \in [0, B]$  is the rotation angle,  $\rho(\beta)$  describes the horizontal distance between the source and the origin of the coordinate system,  $h(\beta)$  denotes the vertical distance from the source to the reference polar coordinate plane. The cylindrical coordinate system can be converted to the Cartesian coordinate system using

$$\begin{cases} x = \rho(\beta) \cos \beta \\ y = \rho(\beta) \sin \beta \\ z = h(\beta). \end{cases} \quad (1)$$

It is assumed that the rotation axis is the  $z$  axis and the interval length of  $\beta$  is not less than  $2\pi$ , that is,  $B \geq 2\pi$ , which means that a specimen is illuminated from all horizontal directions.

In our cone-beam reconstruction, there are mainly two scanning modes, planar and helix-like. A typical case of planar scanning loci is a circle, which is used in the conventional cone-beam reconstruction. A helix-like scanning locus should be used to deal with rod-like specimens. Without loss of generality, a locus turn of the x-ray source can be described by the following parametric equations:

$$\begin{cases} \rho = \rho(\beta) \\ h = h(\beta) \end{cases} \quad (2)$$

where  $\beta \in [0, 2\pi]$ . In the first scanning mode,  $h(\beta) = 0, \beta \in [0, 2\pi]$ . In the second mode,  $h(\beta) \in [z - \frac{h_p}{2}, z + \frac{h_p}{2}]$ ,  $\beta \in [0, 2\pi]$ , where  $z$  is the longitudinal axis coordinate of a specimen transverse slice, and  $h_p$  is the pitch of a helix-like scanning locus. We define the midplane as the reference polar plane in the first scanning mode and the concerned horizontal plane with a longitudinal axis coordinate  $z$  in the second mode.

The fan-beam reconstruction algorithm [12] can be written in the coordinate system  $(x, y)$  as

$$g(x, y) = \frac{1}{2} \int_0^{2\pi} \frac{D_{SO}^2}{(D_{SO} - s)^2} \int_{-\infty}^{\infty} R_{\beta}(p) f\left(\frac{D_{SO} t}{D_{SO} - s} - p\right) \frac{D_{SO}}{\sqrt{D_{SO}^2 + p^2}} dp d\beta \quad (3)$$

where  $(t, s)$  denotes the rotated coordinate system described by

$$t = x \cos \beta + y \sin \beta, \quad s = -x \sin \beta + y \cos \beta$$

$R_{\beta}(p)$  represents the projection data,  $p$  describes a linear detector array intersecting the origin of the reconstruction coordinate system,  $D_{SO}$  denotes the distance between the x-ray source and the origin of the reconstruction coordinate system, and  $f(\cdot)$  is the reconstruction filter defined as

$$f(t) = \int_{-\infty}^{\infty} |w| e^{j2\pi w t} dw.$$

The specimen is assumed to be centered at the origin and along the  $z$ -axis (if it is rod-like).

In the three-dimensional coordinate system  $(x, y, z)$ , the cone-beam reconstruction is performed by tilting the fan out of the midplane, thus changing the coordinate system  $(t, s)$ . A new coordinate system  $(\tilde{t}, \tilde{s})$  is defined to represent the location of a reconstructed point with respect to the tilted fan.

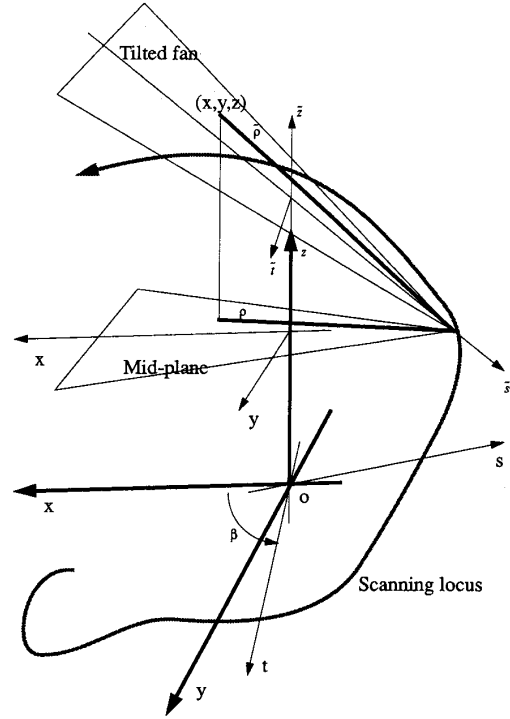


Fig. 3. Schematic diagram illustrating various coordinate systems and variables.

Because of the geometry of the tilted fan, both the source-to-origin distance and the angular differential are changed (Fig. 3). The new source-to-origin distance  $\tilde{\rho}(\beta)$  can be determined using

$$\tilde{\rho}^2(\beta) = \rho^2(\beta) + \zeta^2 \quad (4)$$

where  $\zeta$  is the height of the fan above the center of the midplane as given below

$$\zeta = \frac{\rho(\beta) \tilde{z}(\beta)}{\rho(\beta) - s}. \quad (5)$$

The local coordinate system  $(x, y, \tilde{z}(\beta))$  associated with the angle  $\beta$  is used whose  $\tilde{z}$  coordinate is computed according to

$$\tilde{z}(\beta) = z - h(\beta).$$

Because the fan has been tilted, the equivalent angular increment  $d\tilde{\beta}$  for the tilted fan must be found such that

$$d\beta \rho(\beta) = d\tilde{\beta} \tilde{\rho}(\beta).$$

Then, the equivalent increment of angular rotation  $d\tilde{\beta}$  is

$$d\tilde{\beta} = \frac{d\beta \rho(\beta)}{\sqrt{\rho^2(\beta) + \zeta^2}}. \quad (6)$$

Substituting  $\tilde{\rho}(\beta)$  and  $d\tilde{\beta}$  for  $D_{SO}$  and  $d\beta$  respectively in (3) and denoting two-dimensional projection data as  $R_{\beta}(p, \zeta)$ ,

we obtain the incremental contribution  $dg(x, y, z)$  to the reconstructed voxel  $g(x, y, z)$  as

$$dg(x, y, z) = \frac{1}{2} \frac{\tilde{\rho}^2(\beta)}{(\tilde{\rho}(\beta) - \tilde{s})^2} \int_{-\infty}^{\infty} R_{\beta}(p, \zeta) \cdot f\left(\frac{\tilde{\rho}(\beta)\tilde{t}}{\tilde{\rho}(\beta) - \tilde{s}} - p\right) \frac{\tilde{\rho}(\beta)}{\sqrt{\tilde{\rho}^2(\beta) + p^2}} dp d\beta \quad (7)$$

or

$$dg(x, y, z) = \frac{1}{2} \frac{\tilde{\rho}^2(\beta)}{(\tilde{\rho}(\beta) - \tilde{s})^2} \int_{-\infty}^{\infty} R_{\beta}(p, \zeta) \cdot f\left(\frac{\tilde{\rho}(\beta)\tilde{t}}{\tilde{\rho}(\beta) - \tilde{s}} - p\right) \frac{\rho(\beta)}{\sqrt{\rho^2(\beta) + p^2 + \zeta^2}} dp d\beta. \quad (8)$$

Since

$$\tilde{t} = t, \quad \frac{\tilde{s}}{\tilde{\rho}(\beta)} = \frac{s}{\rho(\beta)} \quad (9)$$

by summing up all incremental contribution, we obtain the following formula for  $g(x, y, z)$ :

$$g(x, y, z) = \frac{1}{2} \int_0^{2\pi} \frac{\rho^2(\beta)}{(\rho(\beta) - s)^2} \int_{-\infty}^{\infty} R_{\beta}(p, \zeta) \cdot f\left(\frac{\rho(\beta)t}{\rho(\beta) - s} - p\right) \frac{\rho(\beta)}{\sqrt{\rho^2(\beta) + p^2 + \zeta^2}} dp d\beta \quad (10)$$

Equation (10) can be referred to as the generalized Feldkamp's cone-beam reconstruction formula [37], [38]. The voxels that are irradiated from all horizontal directions form the *reconstruction region* where reliable reconstruction can be achieved.

The advantages of our generalized cone-beam algorithm are summarized as follows. First, this algorithm allows various scanning loci, giving much more freedom in mechanical and electrical implementation of an x-ray microscope system. For example, it allows a polygonal scanning locus, which eliminates the need of continuously rotating a specimen. Second, it applies to not only sphere-like specimen reconstruction but also rod-shaped specimen reconstruction, which is very common in practical applications. Third, it provides the same computational efficiency and parallelism as Feldkamp's algorithm. Finally,  $z$ -axis artifacts can be uniformized and reduced by our generalized algorithm, if a helix-like scanning locus is used. These points will be illustrated in the following sections.

#### IV. NUMERICAL SIMULATION OF GENERAL CONE-BEAM ALGORITHM

In this section, the digital implementation of our cone-beam reconstruction algorithm is explained. The simulation data and parameters are described. Then, several interesting cone-beam reconstruction algorithms are formulated and simulated as special cases of our cone-beam algorithm.

##### A. Digital Implementation of Our Cone-Beam Algorithm

The key question in the digital implementation of our cone-beam algorithm is how to implement the reconstruction filter  $f(\cdot)$  [12]. Let  $\tau$  denote the sampling interval of projection

data. This means that in Fourier domain the energy outside the frequency interval  $(-W, W)$  is negligible where

$$W = \frac{1}{2\tau}. \quad (11)$$

Since the highest frequency of the projections is finite, we have

$$\begin{aligned} \int_{-\infty}^{\infty} \tilde{R}_{\beta}(w, \zeta) |w| e^{j2\pi w t} dw \\ = \int_{-\infty}^{\infty} \tilde{R}_{\beta}(w, \zeta) F(w) e^{j2\pi w t} dw \end{aligned} \quad (12)$$

where  $\tilde{R}_{\beta}(w, \zeta)$  denotes the one-dimensional Fourier transform of  $R_{\beta}(p, \zeta)$  with respect to  $p$ ,

$$F(w) = |w| b_W(w)$$

and

$$b_W(w) = \begin{cases} 1, & |w| < W \\ 0, & \text{otherwise.} \end{cases}$$

Therefore,  $f(t)$  can be determined as the inverse Fourier transform of  $F(w)$  as follows [12]:

$$f(t) = \frac{1}{2\tau^2} \frac{\sin(\pi t/\tau)}{\pi t/\tau} - \frac{1}{4\tau^2} \left( \frac{\sin(\pi t/2\tau)}{\pi t/2\tau} \right)^2. \quad (13)$$

Since the projection data are measured with a sampling interval of  $\tau$ ,  $f(t)$  needs only be known at discrete points with the same sampling interval. The samples,  $f(n\tau)$ , of  $f(t)$  are given by

$$f(n\tau) = \begin{cases} \frac{1}{4\tau^2}, & n=0; \\ 0, & n \text{ is even}; \\ -\frac{1}{\pi^2 \tau^2 n^2}, & n \text{ is odd.} \end{cases} \quad (14)$$

##### B. Simulation Data and Parameters

A three-dimensional version of Shepp and Logan's head phantom [12] was used in the simulation. The head phantom parameters are listed in Table I. There are ten ellipsoids in the phantom. In Table I,  $x_0, y_0, z_0$  specify the center of an ellipsoid,  $a, b, c$  are the  $x, y, z$  semi-axes respectively,  $\alpha$  is the rotation angle of an ellipsoid (about  $z$  axis), and  $\mu$  is the relative x-ray linear absorption coefficient. The effective x-ray absorption coefficient of a point is the sum of the relative parameters of ellipsoids containing that point. Fig. 4 shows four slices of Shepp and Logan's three-dimensional head phantom. Two are horizontal slices with  $z = -0.25$  (upper-left) and  $z = 0.625$  (upper-right). Two are vertical slices with  $y = -0.105$  (lower-left) and  $y = 0.1$  (lower-right). Note that the real gray level was transformed according to a linear relationship for a better visualization. This transformation linearly maps the interval  $[0.95, 1.05]$  into 256 discrete gray levels. Truncation was done when necessary.

In the numerical simulation, the detector plane is 2.2 by 2.2 with 128 by 128 pixels and was so placed for the ease of computation that its center is at the origin of the reconstruction coordinate system and that its vertical axis is the  $z$ -axis of the coordinate system. One hundred projection images with a  $3.6^\circ$  angular interval were used for the reconstruction, except for the random cone-beam reconstruction where the angular position

TABLE I  
PARAMETERS OF SHEPP AND LOGAN'S THREE-DIMENSIONAL  
HEAD PHANTOM USED IN THE SIMULATION

No.	$x_0$	$y_0$	$z_0$	a	b	c	$\alpha$	$\mu$
1	0.00	0.000	0.000	0.6900	0.920	0.900	0	2.00
2	0.00	0.000	0.000	0.6624	0.874	0.880	0	-0.98
3	-0.22	0.000	-0.250	0.4100	0.160	0.210	108	-0.02
4	0.22	0.000	-0.250	0.3100	0.110	0.220	72	-0.02
5	0.00	0.350	-0.250	0.2100	0.250	0.500	0	0.02
6	0.00	0.100	-0.250	0.0460	0.046	0.046	0	0.02
7	-0.08	-0.650	-0.250	0.0460	0.023	0.020	0	0.01
8	0.06	-0.650	-0.250	0.0460	0.023	0.020	90	0.01
9	0.06	-0.105	0.625	0.0560	0.040	0.100	90	0.02
10	0.00	0.100	0.625	0.0560	0.056	0.100	0	-0.02

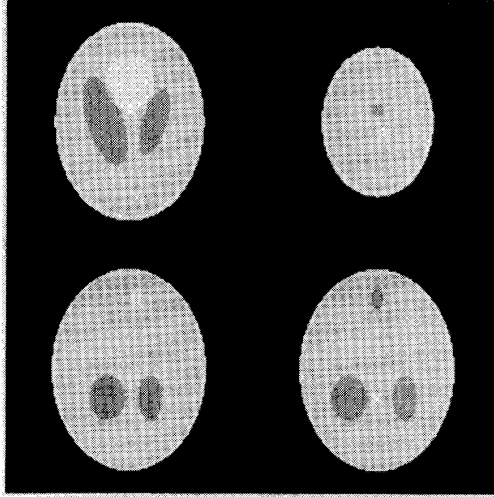


Fig. 4. Four slices of Shepp and Logan's three-dimensional head phantom at  $z = -0.25$  (upper left),  $z = 0.625$  (upper right),  $y = -0.105$  (lower left), and  $y = 0.1$  (lower right), respectively.

is random. Feldkamp's cone-beam reconstruction algorithm is a special case of our algorithm with

$$\begin{cases} \rho = \rho_0 \\ h = 0. \end{cases} \quad (15)$$

Figure 5 shows the reconstructed images using Feldkamp's algorithm with  $\rho_0 = 3$ , corresponding to the four slices shown in Fig. 4. The averaged absolute errors between the original slices and the reconstructed ones were computed as 3.5 (upper-left), 13.3 (upper-right), 13.2 (lower-left), and 13.3 (lower-right) gray levels, respectively.

### C. Polygonal Cone-Beam Reconstruction Algorithm

A polygonal cone-beam reconstruction algorithm is obtained [32] by setting

$$\begin{cases} \rho = \frac{\rho_0}{\cos(\beta - \frac{2\pi}{N_S} \lfloor \frac{N_S \beta}{2\pi} + 0.5 \rfloor)} \\ h = 0 \end{cases} \quad (16)$$

where  $\rho_0$  is the minimum distance between the source and the origin,  $N_S$  is the number of sides of the scanning polygon, and  $\lfloor \cdot \rfloor$  represents a floor function. The polygonal cone-beam reconstruction algorithm is used to reduce the number of recalibrations of the mechanical axis position.

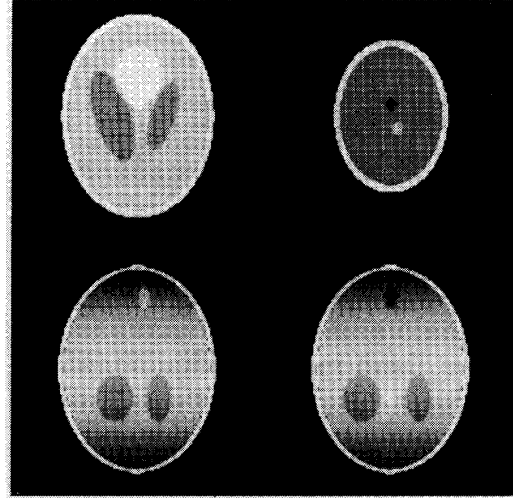


Fig. 5. Four reconstructed slices obtained using Feldkamp's cone-beam reconstruction algorithm when  $\rho_0 = 3$ , corresponding to the four slices of the phantom shown previously.

For tomographic imaging, a large number of two-dimensional projection images must be recorded at various orientations. The specimen therefore must be rotated, and a mechanical stage is installed for this purpose. Because the variation of rotation axis position of the mechanical stage is one of the major error sources in microtomography, an elaborate feed-back system is required to minimize the error. However, experiments showed that the calibration of the rotation axis position is both time-consuming and complicated. On the other hand, the x-ray source of our microscope system can be precisely moved by steering the e-beam electromagnetically. With the polygonal algorithm, the number of the stage rotation can be greatly reduced. The straight line portions of the polygon are achieved by the x-ray source movement and the number of the polygon sides determines the number of the stage rotations.

Figure 6 shows four reconstructed images obtained using the polygonal cone-beam reconstruction algorithm with  $\rho_0 = 3$  and  $N_S = 8$ . The averaged absolute errors between the original and reconstructed slices are almost the same as those obtained with Feldkamp's algorithm. We have proved that the polygonal algorithm will give exact reconstruction on the midplane, if the scanning polygon has an even number of sides.

### D. Multiple Cone-Beam Reconstruction Algorithm

In this algorithm, Feldkamp's or the polygonal cone-beam algorithm is applied on different sets of cone-beam projection data captured with a set of planar scanning loci (Fig. 7) [39]. We only use the polygonal algorithm here. In general, if  $n$  x-ray sources are available, the interested reconstruction region can be horizontally divided equally into  $n$  segments and the central horizontal plane of each segment contains a polygonal scanning locus. Let us consider a twin cone-beam reconstruction algorithm. For a given slice with a vertical coordinate  $z$ , the closest planar scanning locus can

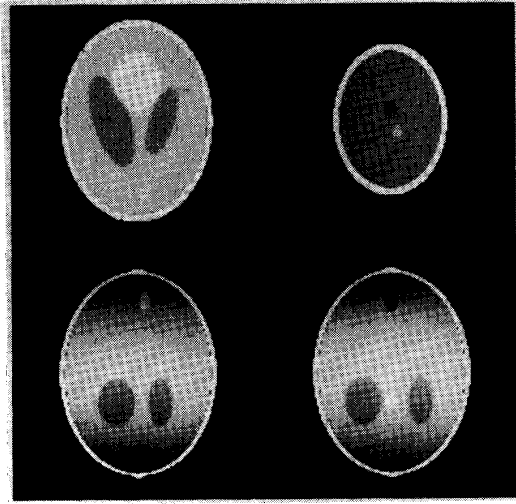


Fig. 6. Four reconstructed slices obtained using the polygonal cone-beam reconstruction algorithm with  $\rho_0 = 3$  and  $N_S = 8$ , corresponding to the four slices of the phantom shown previously.

be described as

$$\begin{cases} \rho = \frac{\rho_0}{\cos(\beta - \frac{2\pi}{N_S} [\frac{N_S \beta}{2\pi} + 0.5])} \\ h = \text{sign}(z) \frac{d}{2} \end{cases} \quad (17)$$

where  $\rho_0$  is a constant,  $N_S$  is the number of the scanning polygon sides,  $d$  is a vertical distance between the scanning planes, and  $\text{sign}(\cdot)$  represents the sign function. This algorithm is used to improve the off-mid-plane reconstruction accuracy and to deal with rod-shaped specimens, which are commonly found in biological and material science.

Two reasonable strategies for the estimation of voxel values are (1) to interpolate two voxel values obtained from the upper- and lower-cone-beam reconstructions; and (2) to select the voxel value obtained from the cone-beam reconstruction whose midplane is the nearest to the voxel. In the simulation, we used the second. Figure 8 shows the reconstructed images obtained using the twin polygonal cone-beam algorithm with  $\rho_0 = 3$ ,  $N_S = 8$ , and  $d = 1.25$ , respectively. Note that two midplanes used here are planes  $z = 0.625$  and  $z = -0.625$ , while the midplane used for Feldkamp's algorithm and the polygonal algorithm is the plane  $z = 0$ . The lower two images show clearly horizontal dark stripes. The averaged absolute errors between the original and reconstructed slices are 5.3 (upper-left), 2.4 (upper-right), 7.1 (lower-left) and 7.2 (lower-right) gray levels respectively. This multiple algorithm reduces the reconstruction error of vertical slices, which is due to the fact that the reconstruction of off-midplane structures is improved.

#### E. Helical Cone-Beam Reconstruction Algorithm

In order to handle rod-shaped specimens, a helical cone-beam reconstruction algorithm can be designed. Contrast to Feldkamp's algorithm where the scanning locus of an x-ray source is a circle, the helical cone-beam reconstruction algorithm requires the translation of the x-ray source and the

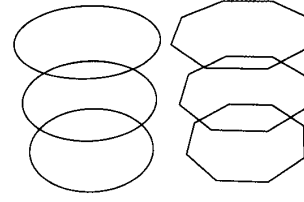


Fig. 7. The scanning locus in the multiple cone-beam reconstruction.

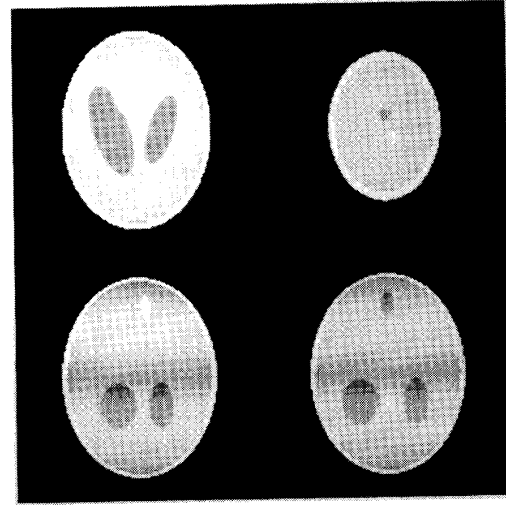


Fig. 8. Four reconstructed slices obtained using the twin polygonal cone-beam reconstruction algorithm with  $\rho_0 = 3$ ,  $N_S = 8$ , and  $d = 1.25$ , respectively, corresponding to the four slices of the phantom shown previously.

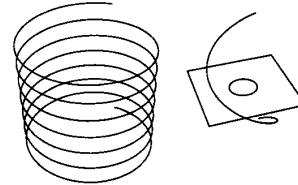


Fig. 9. The scanning locus in the helical approach and a mid-plane.

simultaneous rotation of the specimen, hence the motion locus of the x-ray source is a continuous helix in the specimen coordinate system. A helical turn (Fig. 9, right) is referred to as the portion of a helix generated by varying  $\beta$  continuously for  $2\pi$ . For any horizontal slice of the specimen, it is assumed that such a helical turn can always be found that the turn is divided by the concerned slice into upper and lower halves. Projection images collected from this turn are used to reconstruct the specimen slice (Fig. 9.) A scanning turn in this scanning mode can be formulated as

$$\begin{cases} \rho = \rho_0 \\ h = \frac{h_p \beta}{2\pi} \end{cases} \quad (18)$$

where  $\rho_0$  is a constant and  $h_p$  is the pitch of the helix turn [40].

Compared with the multiple cone-beam algorithm, the helical cone-beam algorithm results in a more uniform error distribution along the  $z$  axis. Figure 10 shows four reconstructed

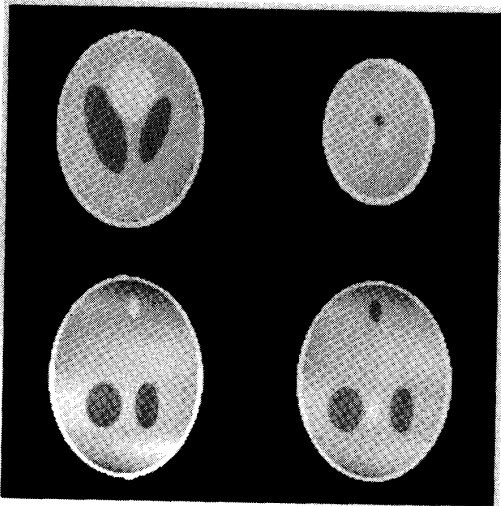


Fig. 10. Four reconstructed slices obtained using the helical cone-beam reconstruction algorithm with  $\rho = 3$  and  $h_p = 1.25$ , corresponding to the four slices of the phantom shown previously.

images obtained using the helical cone-beam reconstruction algorithm with  $\rho_0 = 3$  and  $h_p = 1.25$ . The vertical distance ( $= 1.25$ ) between adjacent scanning planes in the multiple cone-beam algorithm is the same as the pitch of the helical scanning locus. It can be observed that the horizontal dark stripes shown in two lower images of Fig. 8 have been eliminated. The averaged absolute errors between the original and reconstructed slices are 4.3 (upper left), 3.4 (upper right), 6.8 (lower left) and 6.1 (lower right) gray levels, respectively. These data show that the helical algorithm does uniformize and reduce the reconstruction errors between the original and reconstructed vertical slices. The error for the upper-right image ( $= 3.4$ ) is higher than that ( $= 2.4$ ) of the multiple cone-beam algorithm, because this slice is on one of the midplanes in the multiple cone-beam reconstruction algorithm.

### F. 3-D Broken-Line Cone-Beam Reconstruction Algorithm

The above helical cone-beam reconstruction utilizes a smooth and simultaneous rotation and translation of the specimen with respect to the incident x-ray cone. A three-dimensional broken-line cone-beam algorithm can be constructed from the combination of the polygonal cone-beam algorithm and the helical cone-beam algorithm. A turn of the scanning locus required by this hybrid algorithm is described by

$$\begin{cases} \rho = \frac{\rho_0}{\cos(\beta - \frac{2\pi}{N_S} [\frac{N_S \beta}{2\pi} + 0.5])} \\ h = \frac{h_p \beta}{2\pi} \end{cases} \quad (19)$$

where  $\rho_0$  is a constant,  $N_S$  is the number of the scanning polygon sides, and  $h_p$  is the pitch of the scanning locus. The helix in the helical reconstruction becomes a sequence of connected short lines which segments a helix (Fig. 11).

Figure 12 shows four reconstructed images obtained using the three-dimensional broken-line cone-beam reconstruction algorithm, with  $\rho_0 = 3$ ,  $N_S = 8$  and  $h_p = 1.25$  respectively.

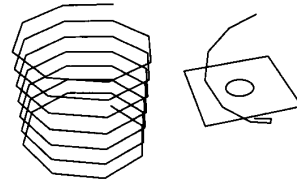


Fig. 11. The scanning locus in the broken-line approach and a mid-plane.

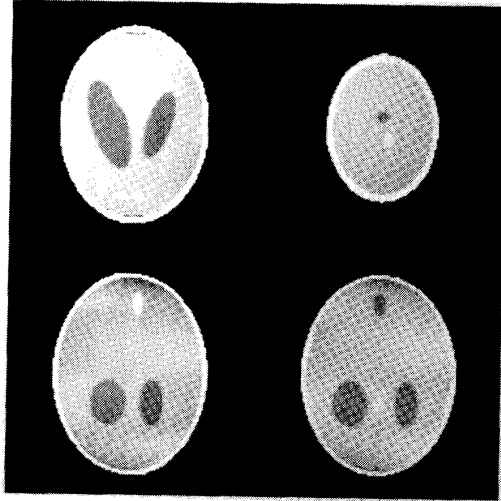


Fig. 12. Four reconstructed slices obtained using the three-dimensional broken-line cone-beam reconstruction algorithm, when  $\rho_0 = 3$ ,  $N_S = 8$ , and  $h_p = 1.25$ , respectively, corresponding to the four slices of the phantom shown previously.

The averaged absolute errors between the original and reconstructed slices are 4.1 (upper left), 3.5 (upper right), 6.7 (lower left), and 5.7 (lower right) gray levels respectively. Similar remarks can be made as on the helical algorithm. The accuracy of the broken-line algorithm is very close to that of the helical algorithm. This algorithm will eventually be implemented for our x-ray microscope system.

### G. 3-D Dashed-Line Cone-Beam Reconstruction Algorithm

The three-dimensional dashed-line algorithm is similar to the broken-line algorithm, except that the scanning turn of the three-dimensional dashed-line cone-beam algorithm is described as

$$\begin{cases} \rho = \frac{\rho_0}{\cos(\beta - \frac{2\pi}{N_S} [\frac{N_S \beta}{2\pi} + 0.5])} \\ h = \frac{h_p}{N_S} \lfloor \frac{N_S \beta}{2\pi} \rfloor \end{cases} \quad (20)$$

where  $\rho_0$  is a constant,  $N_S$  is the number of the scanning polygon sides, and  $h_p$  is the counterpart of the pitches used in helical and broken-line algorithms. The difference between the broken-line algorithm and the dashed-line algorithm lies in that the inclined lines in the former become horizontal lines in the latter. Hence the scanning locus required by the dashed-line algorithm is similar to "winding stairs" as shown in Fig. 13.

The dashed-line algorithm is superior to the broken-line algorithm when the relative motion of a specimen along the  $z$ -

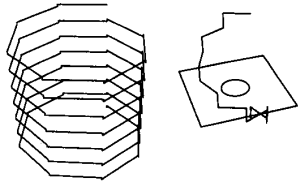


Fig. 13. The scanning locus in the dashed-line approach and a mid-plane.

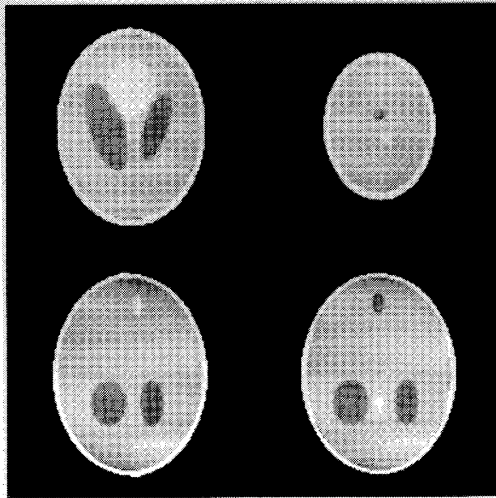


Fig. 14. Four reconstructed slices obtained using the three-dimensional dashed-line cone-beam reconstruction algorithm, when  $\rho_0 = 3$ ,  $N_S = 8$ , and  $h_p = 1.25$ , respectively, corresponding to the four slices of the phantom shown previously.

axis is implemented by shifting the mechanical stage, allowing a much larger dynamic range for translating a rod-shaped specimen along the  $z$ -axis but producing greater mechanical errors. The dashed-line algorithm can greatly reduce the number of the mechanical stepping of the stage, and thus simplify the recalibration process needed for the reconstruction.

Figure 14 shows four reconstructed images obtained using the three-dimensional dashed-line cone-beam reconstruction algorithm, with  $\rho_0 = 3$ ,  $N_S = 8$  and  $h_p = 1.25$  respectively. The averaged absolute errors between the original and the reconstructed ones are 4.1 (upper left), 3.3 (upper right), 6.4 (lower left) and 5.8 (lower right) gray levels respectively. Similar comments can be made as on the broken-line algorithm. This algorithm will also be implemented for our x-ray microscope system.

#### H. Random Cone-Beam Reconstruction Algorithm

We can also reconstruct the three-dimensional image of a specimen with a random scanning locus, which is modeled by

$$\begin{cases} \rho = \rho_0 + c_\rho \cdot \text{random}() \\ h = c_h \cdot \text{random}() \end{cases} \quad (21)$$

where  $\rho_0$ ,  $c_\rho$  and  $c_h$  are constants, and  $\text{random}()$  is a  $[-0.5, 0.5]$  uniformly distributed random variable. Unlike in the previous cases where  $\beta$  was sampled evenly,  $\beta$  was

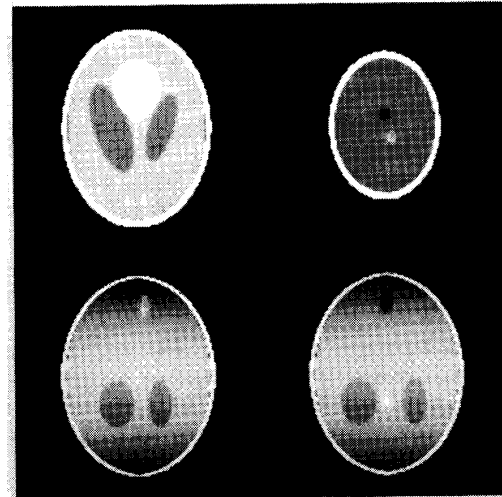


Fig. 15. Four reconstructed slices obtained using the random algorithm with  $\rho_0 = 3$ ,  $c_\rho = 1.0$ , and  $c_h = 0.5$ , respectively, corresponding to the four slices of the phantom shown previously.

sampled randomly here. The random algorithm was designed for testing the stability of our cone-beam algorithm in case that  $\rho(\beta)$  does not describe a curve symmetric with respect to the origin.

Figure 15 shows four reconstructed images obtained using the random algorithm with  $\rho_0 = 3$ ,  $c_\rho = 1.0$ , and  $c_h = 0.5$ , respectively. The averaged absolute errors between the original and reconstructed slices are 4.0 (upper left), 13.4 (upper right), 13.5 (lower left), and 13.4 (lower right) gray levels, respectively. Compared with the results obtained for Feldkamp's algorithm, the errors increased only slightly. This indicates that our cone-beam algorithm is quite robust.

#### V. ANALYTIC PROPERTIES OF GENERAL CONE-BEAM ALGORITHM

Since our cone-beam algorithm is derived heuristically, like Feldkamp's algorithm, it is desirable to have some analytic properties. Assume that the reconstruction is performed using projection data collected from a turn of a scanning locus, three analytic properties of our algorithm are given in this section. These properties further justify the algorithm.

##### A. Reconstruction Is Exact on Midplane

When our cone-beam algorithm is applied in a planar scanning mode, a derivative-free noncircular fan-beam reconstruction formula is obtained by only considering the midplane reconstruction. It has been proved that the extended fan-beam formula is exact if some conditions are satisfied [41]<sup>1</sup>. These conditions require that the scanning locus be differentiable almost everywhere with respect to the rotation angle, be symmetric with respect to the origin of the reconstruction

<sup>1</sup> An anonymous reviewer helped us correct an error contained in (23) in [41]. The work reported in [41] will be published in the October 1993 issue of *IEEE Trans. on Image Processing*.



coordinate system, and the mapping from fan-beam data to parallel-beam data is one-to-one (that is, the direction tangent to the locus stay outside of the fan delimited by the object support). At least for cone-beam x-ray microtomography, these conditions are sufficiently general. For example, polygons of even sides meet these requirements.

The main idea used in the proof of [41] is that the extended fan-beam reconstruction formula can be expressed in terms of parallel-beam projection data. If the correct parallel-beam reconstruction formula could be obtained by rewriting the new fan-beam formula through transforming fan-beam data into parallel-beam data, then the new formula is proved.

The new formula is simpler than other published ones, as it is the same as the conventional equispacial one [12], except that the source-to-origin distance depends on the rotation angle. The new formula is also more stable, as it involves no derivative of the locus.

### B. Vertical Integral of Reconstruction Is Exact

It has been proved that the vertical integral of the PSF  $s(x, y, z; x_0, y_0, z_0)$  of our cone-beam reconstruction algorithm is a two-dimensional  $\delta$  function  $\delta(x - x_0)\delta(y - y_0)$  in [42], where some intermediate integrals should be interpreted in the generalized sense when necessary [43], [12], [35], [10]. Using this interesting property of the PSF, it can be shown as follows that the vertical integral of a reconstructed 3-D image is equal to that of the real specimen image [42].

The reconstructed three-dimensional image can be expressed in terms of the spatially varying PSF as

$$g(x, y, z) = \int_{-\infty}^{\infty} \int_{-\infty}^{\infty} \int_{-\infty}^{\infty} i(u, v, w) s(x, y, z; u, v, w) du dv dw \quad (22)$$

where  $i(x, y, z)$  is the real specimen image. Therefore,

$$\begin{aligned} & \int_{-\infty}^{\infty} g(x, y, z) dz \\ &= \int_{-\infty}^{\infty} \int_{-\infty}^{\infty} \int_{-\infty}^{\infty} i(u, v, w) \\ & \quad \times \left[ \int_{-\infty}^{\infty} s(x, y, z; u, v, w) dz \right] du dv dw \\ &= \int_{-\infty}^{\infty} \int_{-\infty}^{\infty} \int_{-\infty}^{\infty} i(u, v, w) \delta(x - u) \delta(y - v) du dv dw \\ &= \int_{-\infty}^{\infty} i(x, y, w) dw \\ &= \int_{-\infty}^{\infty} i(x, y, z) dz. \end{aligned} \quad (23)$$

### C. Reconstruction Is Exact If $i(x, y, z)$ Is Independent of $z$

Let us assume that the two-dimensional scanning curve described by  $\rho(\beta), \beta \in [0, 2\pi]$  meet the requirements of our extended fan-beam reconstruction formula [41]. For convenience,

our cone-beam reconstruction formula is repeated here:

$$\begin{aligned} g(x, y, z) &= \frac{1}{2} \int_0^{2\pi} \frac{\rho^2(\beta)}{(\rho(\beta) - s)^2} \\ & \quad \int_{-\infty}^{\infty} R_\beta(p, \zeta) f\left(\frac{\rho(\beta)t}{\rho(\beta) - s} - p\right) \frac{\rho(\beta)}{\sqrt{\rho^2(\beta) + p^2 + \zeta^2}} dp d\beta. \end{aligned} \quad (24)$$

We can rewrite the above formula as

$$\begin{aligned} g(x, y, z) &= \frac{1}{2} \int_0^{2\pi} \frac{\rho^2(\beta)}{(\rho(\beta) - s)^2} \\ & \quad \int_{-\infty}^{\infty} S_\beta(p, z) f\left(\frac{\rho(\beta)t}{\rho(\beta) - s} - p\right) \frac{\rho(\beta)}{\sqrt{\rho^2(\beta) + p^2}} dp d\beta \end{aligned} \quad (25)$$

where

$$\begin{aligned} S_\beta(p, z) &= R_\beta(p, \zeta) \frac{\sqrt{\rho^2(\beta) + p^2}}{\sqrt{\rho^2(\beta) + p^2 + \zeta^2}} \\ \zeta &= \frac{\rho(\beta)\tilde{z}(\beta)}{\rho(\beta) - s}, \text{ and } \tilde{z}(\beta) = z - h(\beta). \end{aligned}$$

On the other hand,

$$\begin{aligned} i(x, y, z) &= \frac{1}{2} \int_0^{2\pi} \frac{\rho^2(\beta)}{(\rho(\beta) - s)^2} \\ & \quad \int_{-\infty}^{\infty} T_\beta(p, z) f\left(\frac{\rho(\beta)t}{\rho(\beta) - s} - p\right) \frac{\rho(\beta)}{\sqrt{\rho^2(\beta) + p^2}} dp d\beta \end{aligned} \quad (26)$$

where  $T_\beta(p, z)$  is the fan-beam projection data of the specimen slice at the vertical axis coordinate  $z$ .  $S_\beta(p, z)$  can be considered as an approximation to  $T_\beta(p, z)$ .  $S_\beta(p, z)$  is found by multiplying  $R_\beta(p, \zeta)$  with a projection factor  $\frac{\sqrt{\rho^2(\beta) + p^2}}{\sqrt{\rho^2(\beta) + p^2 + \zeta^2}}$ , which is the cosine of the angle (depending on  $p$ ) between fan rays corresponding to  $R_\beta(p, \zeta)$  and  $T_\beta(p, z)$  respectively. Note that  $i(x, y, z)$  is the true specimen image function, because our extended fan-beam reconstruction algorithm is exact in this case. When  $i(x, y, z)$  is independent of  $z$ , it is evident that  $S_\beta(p, z) = T_\beta(p, z)$ , hence, the reconstruction is exact [44]. The above analysis also provides clues on why the helix-like scanning loci work better than multiple planar scanning loci. Generally speaking,  $S_\beta(p, z)$  obtained with a helix-like scanning locus approximates  $T_\beta(p, z)$  better.

After a source point and a reconstruction point are given, there are infinite many ways to select tilted fans. The rationale behind our selection (and Feldkamp's selection as well) can be explained as follows. In our scheme, fans are tilted horizontally so that modified projection data can be imagined as being approximate to the imaginary horizontal fan-beam projection data, and if  $i(x, y, z)$  is independent of  $z$ , the reconstruction will be exact.

## VI. CONCLUSION AND DISCUSSION

Our generalized cone-beam reconstruction algorithm presented in this paper takes full advantage of the hardware characteristics of the x-ray microscope system being developed at SUNY at Buffalo, overcomes the limitations of Feldkamp's cone-beam reconstruction algorithm and maintains its high computational efficiency and parallelism. Our cone-beam algorithm provides a framework allowing various scanning loci suitable for different applications. This algorithm not only gives satisfactory reconstruction images but also has the following three nice properties if a scanning locus meets some conditions. First, the reconstruction with a planar scanning locus gives the exact result on midplane. Second,

$$\int_{-\infty}^{\infty} g(x, y, z) dz = \int_{-\infty}^{\infty} i(x, y, z) dz \quad (27)$$

where  $g(x, y, z)$  and  $i(x, y, z)$  are three-dimensional reconstructed and actual images respectively. Third, if  $i(x, y, z)$  is independent of  $z$ , then

$$g(x, y, z) = i(x, y, z). \quad (28)$$

Also, if a helix-like scanning locus is used,  $z$ -axis artifacts will be uniformized and reduced.

Scanning loci used by the polygonal, multiple, dashed-line, and random algorithms do not satisfy Tuy's or Smith's conditions for exact reconstruction [14], [35], [36], [10], therefore, an approximation cannot be avoided. Our approximation has been justified in this paper. On the other hand, helical and broken-line scanning loci do meet the requirements for the exact reconstruction. Our algorithm does not take advantage of this theoretical potential. The exact reconstruction schemes [35], [36], [10] could be used in this case. However, these exact algorithms are computationally inefficient. On the other hand, as shown in this paper, our approximate algorithms are quite accurate. Although Smith also proposed a both exact and efficient scheme [10, 33], as mentioned earlier, the conditions for his exact and efficient algorithm are too restrictive.

Our cone-beam reconstruction algorithm can be considered as being derived based on our derivative-free noncircular fan-beam reconstruction formula [41]. Using our methodology, two other noncircular fan-beam reconstruction formulas [28], [29], [45], [46] can also be extended to cone-beam reconstruction with various non-planar scanning loci. Although a derivative of the scanning locus will be contained in these cone-beam reconstruction formulas, it can be readily and similarly proved that all three analytic properties described in Section V still hold. By doing so, we actually extend Gullberg's cone-beam reconstruction formula [29] into a general case. In fact, Gullberg *et al.* extended Feldkamp's algorithm *horizontally*, while we did it both *horizontally* and *vertically*.

In order to study the reconstruction accuracy of our cone-beam algorithm, a systematic and quantitative error analysis is being performed [44], [47]. Relevant results will be reported in the future.

## ACKNOWLEDGMENT

The authors are grateful to anonymous reviewers for their valuable comments. The photos in this paper were prepared at the Division of Radiology Research, Mallinckrodt Institute of Radiology, Washington University School of Medicine, with the technical assistance of Professor M. W. Vannier, Mr. B. Brunsden, Mr. N. Hente, Mr. R. Knapp, and Mr. R. Walkup.

## REFERENCES

- [1] L. A. Feldkamp, L. C. Davis, and J. W. Kress, "Practical cone-beam algorithm," *J. Opt. Soc. Am.*, vol. 1 (A), pp. 612-619, 1984.
- [2] P. C. Cheng, S. P. Newberry, H. G. Kim, and M. D. Wittman, "X-ray contact microradiography and shadow projection x-ray microscopy," *Europ. J. Cell Biology*, vol. 48, no. 25, pp. 169-172, 1989.
- [3] P. C. Cheng, S. P. Newberry, H. G. Kim, M. D. Wittman, and I.-S. Hwang, "X-ray contact microradiography and shadow projection microscopy," in *Modern microscopy* (P. Duke and A. Michette, eds.), pp. 87-117. New York: Plenum Press, 1990.
- [4] G. Schmahl and P. C. Cheng, "X-ray microscopy," in *Handbook on Synchrotron Radiation* (T.S. E.E. Koch and H. Winick, eds.), vol. 4, pp. 481-536. New York: North-Holland, 1991.
- [5] P. C. Cheng and G. J. Jan, *X-ray Microscopy — Instrumentation and Biological Applications*. New York: Springer-Verlag, 1987.
- [6] P. C. Cheng, D. M. Shinozaki, T. H. Lin, S. P. Newberry, R. Sridhar, W. Tang, M. T. Chen, and L. H. Chen, "X-ray shadow projection microscopy and microtomography," in *x-ray microscopy — III*, A. Michette, G. R. Morris, and C. J. Buckley, eds. Berlin: Springer-Verlag, 1991.
- [7] P. C. Cheng, T. H. Lin, D. M. Shinozaki, and S. P. Newberry, "Projection microscopy and microtomography using x-rays," *J. Scanning Microscopy*, vol. 13 (1), pp. 10-11, 1991.
- [8] G. Wang, T. H. Lin, P. C. Cheng, D. M. Shinozaki, and S. P. Newberry, "X-ray projection microscopy and cone-beam microtomography," in *Proc. SPIE*, vol. 1398, pp. 180-190, 1991.
- [9] W. Graeff and K. Engelke, "Microradiography and microtomography," in *Handbook on Synchrotron Radiation*, T.S. E.E. Koch and H. Winick, eds., vol. 4, pp. 361-405. New York: North-Holland, 1991.
- [10] B. D. Smith, "Cone-beam tomography: recent advances and a tutorial review," *Opt. Engineering*, vol. 29, pp. 524-534, May 1990.
- [11] R. M. Lewitt, "Reconstruction algorithms: Transform methods," *Proc. IEEE*, vol. 71, pp. 390-408, Mar 1983.
- [12] A. C. Kak and M. Slaney, *Principles of Computerized Tomographic Imaging*. Piscataway, NJ: IEEE Press, 1987.
- [13] A. A. Kirillov, "On a problem of I. M. Gel'fand," *Sov. Math. Dokl.*, vol. 2, pp. 268-269, 1961. English translation.
- [14] H. K. Tuy, "An inversion formula for cone-beam reconstruction," *SIAM J. Appl. Math.*, vol. 43, pp. 546-552, 1983.
- [15] C. Hamaker, D. C. Solmon, and S. L. Wagner, "The divergent beam x-ray transform," *Rocky Mountain J. Math.*, vol. 10, pp. 253-259, 1980.
- [16] O. Nalcioglu and Z. H. Cho, "Reconstruction of 3-D objects from cone-beam projections," *Proc. IEEE*, vol. 66, pp. 1584-1585, 1978.
- [17] R. V. Denton, B. Friedlander, and A. J. Rockmore, "Direct three-dimensional image reconstruction from divergent rays," *IEEE Trans. Nucl. Sci.*, vol. NS-26, pp. 4695-4703, 1979.
- [18] K. T. Smith, D. C. Solomon, and S. L. Wagner, "Inversion formulas for the x-ray transform," *Rocky Mount J. Math.*, vol. 10, pp. 253-283, 1980.
- [19] K. T. Smith, "Reconstruction formulas in computed tomography," in *Proc. Symposium on Applied Mathematics*, vol. 27, pp. 7-23, Am. Math. Soc., 1982.
- [20] J. Imiya and H. Ogawa, "A direct method of image reconstruction from its line integrals by cone-beam x-rays," in *Proc. Int. Joint Alpine Symp. on Medical Computing, Graphics Image Communication, and Clinical Advances in Neuro CT/NMR*, IEEE, pp. 95-101, 1984.
- [21] F. C. Peyrin, "The generalized backprojection theorem for cone-beam reconstruction," *IEEE Trans. Nucl. Sci.*, vol. NS-32, pp. 1512-1519, 1985.
- [22] G. T. Herman, *Image Reconstruction from Projections*. New York: Academic Press, 1980.
- [23] R. M. Lewitt and M. R. McKay, "Description of a software package for computing cone-beam x-ray projections of time-varying structures, and for dynamic three-dimensional image reconstruction," Tech. Rep. MIPG45, Dept. of CS, SUNY/Buffalo, May 1980.
- [24] R. A. Robb, A. H. Lent, B. K. Gilbert, and A. Chu, "The dynamic spatial reconstructor," *J. Med. Syst.*, vol. 4, pp. 253-288, 1980.

- [25] P. Grangeat, "Description of a 3D reconstruction algorithm for diverging x-ray beam," in *Radiology Society of North America Conf. Proc.*, 1985.
- [26] P. Grangeat, "3D reconstruction algorithm for diverging x-ray beams," in *CAR '85 Conf. Proc.*, 1985.
- [27] P. Sire, P. Grangeat, P. Lemasson, P. Meulenec, and P. Rizo, "NDT applications of the 3D RADON transform algorithm for cone beam reconstruction," in *Proc. Fall Meeting of the Material Research Soc.* (Boston), 1990.
- [28] G. T. Gullberg, G. L. Zeng, P. E. Christian, B. M. W. Tsui, and H. T. Morgan, "Single photon emission computed tomography of the heart using cone beam geometry and noncircular detector rotation," in *Proc. 11th Int. Conf. on Information Processing in Medical Imaging*, pp. 123-138, 1991.
- [29] G. T. Gullberg and G. L. Zeng, "A cone-beam filtered backprojection reconstruction algorithm for cardiac single photon emission computed tomography," *IEEE Trans. Med. Imag.*, vol. 11, no. 1, pp. 91-101, 1992.
- [30] R. J. Jaszcak, K. L. Greer, and R. E. Coleman, "SPECT using a specially designed cone beam collimator," *J. Nuclear Med.*, vol. 29, pp. 1398-1405, 1988.
- [31] R. J. Jaszcak, C. E. Floyd, S. H. Manglos, K. L. Greer, and R. E. Coleman, "Cone beam collimation for single photon emission computed tomography: Analysis, simulation, and image reconstruction using filtered backprojection," *Med. Phys.*, vol. 13, pp. 484-489, 1986.
- [32] G. Wang, T. H. Lin, P. C. Cheng, and D. M. Shinozaki, "A polygonal cone-beam reconstruction algorithm for x-ray microtomography," *J. Scanning Microscopy*, vol. 13 (I), pp. 126-128, 1991.
- [33] B. D. Smith, "Advances in cone-beam tomography for the analysis of materials," in *Proc. Symp. on Advanced Tomographic Imaging Methods for the Analysis of Materials*, Nov. 1990.
- [34] B. D. Smith, "Cone-beam convolution formula," *Comput. Bio. Med.*, vol. 13, pp. 81-87, 1983.
- [35] B. D. Smith, "Image reconstruction from cone-beam projections: necessary and sufficient conditions and reconstruction methods," *IEEE Trans. Med. Imag.*, vol. MI-4, pp. 14-28, 1985.
- [36] B. D. Smith, *Computer-aided tomographic imaging from cone-beam data*. Ph.D. dissertation, Univ. of Rhode Island, 1987.
- [37] G. Wang, T. H. Lin, P. C. Cheng, D. M. Shinozaki, and H. Kim, "Scanning cone-beam reconstruction algorithms for x-ray microtomography," in *Proc. SPIE*, vol. 1556, pp. 99-113, 1991.
- [38] G. Wang, T. H. Lin, H. G. Kim, D. M. Shinozaki, and P. C. Cheng, "Cone-beam x-ray microtomography," chapter 9 in *Multi-dimensional Microscopies*, P. C. Cheng, T. H. Lin, and W. L. Wu, eds. New York: Springer-Verlag, in press, 1993.
- [39] T. H. Lin, G. Wang, P. C. Cheng, and D. M. Shinozaki, "A multiple cone-beam projection algorithm for x-ray microtomography," in *X-ray Microscopy—III* (A. Michette, G. R. Morrison, and C. J. Buckley, eds.), pp. 296-300. Berlin: Springer-Verlag, 1991.
- [40] T. H. Lin, G. Wang, P. C. Cheng, and D. M. Shinozaki, "A helical cone-beam reconstruction algorithm for x-ray microtomography," *J. Scanning Microscopy*, vol. 13 (I), pp. 11-13, 1991.
- [41] G. Wang, T. H. Lin, and P. C. Cheng, "A new extended fan-beam reconstruction formula," in *Proc. SPIE*, vol. 1660, pp. 262-273, 1992.
- [42] G. Wang, T. H. Lin, P. C. Cheng, and D. M. Shinozaki, "Point spread function of the general cone-beam x-ray reconstruction formula," *J. Scanning Microscopy*, vol. 14, no. 4, pp. 187-193, 1992.
- [43] X. H. Yan and R. M. Leahy, "Derivation and analysis of a filtered backprojection algorithm for cone beam projection data," *IEEE Trans. Med. Imag.*, vol. 10, no. 3, pp. 462-472, 1991.
- [44] G. Wang, T. H. Lin, P. C. Cheng, and D. M. Shinozaki, "Preliminary error analysis on the general cone-beam reconstruction algorithm," in *Proc. SPIE*, vol. 1660, pp. 274-285, 1992.
- [45] F. S. Weinstein, "Formation of images using fan beam scanning and noncircular source motion," *J. Opt. Soc. Amer.*, vol. 70, pp. 931-935, 1980.
- [46] B. D. Smith, "Derivation of the extended fan-beam formula," *IEEE Trans. Med. Imag.*, vol. MI-4, pp. 177-184, 1985.
- [47] T. H. Lin, G. Wang, and P. C. Cheng, "Error analysis of the general cone-beam reconstruction algorithm for x-ray microtomography," *J. Scanning Microscopy, Suppl. II (Addendum)*, pp. 20-23, 1992.